

# The spin-wave spectrum of the Jahn-Teller system $\text{LaTiO}_3$

Robert Schmitz,<sup>1</sup> Ora Entin-Wohlman,<sup>2</sup> Amnon Aharony,<sup>2</sup> A. Brooks Harris,<sup>3</sup> and Erwin Müller-Hartmann<sup>1</sup>

<sup>1</sup>*Institut für Theoretische Physik, Universität zu Köln, Zùlpicher Straße 77, 50937 Köln, Germany*

<sup>2</sup>*School of Physics and Astronomy, Raymond and Beverly Sackler Faculty of Exact Sciences, Tel Aviv University, Tel Aviv 69978, Israel*

<sup>3</sup>*Department of Physics and Astronomy, University of Pennsylvania, Philadelphia, Pennsylvania 19104, USA*  
(September 17, 2018)

We present an analytical calculation of the spin-wave spectrum of the Jahn-Teller system  $\text{LaTiO}_3$ . The calculation includes all superexchange couplings between nearest-neighbor Ti ions allowed by the space-group symmetries: The isotropic Heisenberg couplings and the antisymmetric (Dzyaloshinskii-Moriya) and symmetric anisotropies. The calculated spin-wave dispersion has four branches, two nearly degenerate branches with small zone-center gaps and two practically indistinguishable high-energy branches having large zone-center gaps. The two lower-energy modes are found to be in satisfying agreement with neutron-scattering experiments. In particular, the experimentally detected approximate isotropy in the Brillouin zone and the small zone-center gap are well reproduced by the calculations. The higher-energy branches have not been detected yet by neutron scattering but their zone-center gaps are in satisfying agreement with recent Raman data.

PACS numbers: 71.10.-w, 71.27.+a, 75.30.Ds, 75.50.Ee

## I. INTRODUCTION

The orthorhombic perovskite  $\text{LaTiO}_3$  has long been considered as a typical antiferromagnetic Mott insulator ( $T_N = 146\text{ K}$ ). Albeit its rather small ordered magnetic moment,  $0.46\text{--}0.57\mu_B$ ,<sup>1,2</sup> experimentally it seems not very different from a conventional Heisenberg antiferromagnetic insulator. Indeed, the spin-wave spectrum measured by Keimer *et al.*<sup>1</sup> is well described by a nearest-neighbor superexchange coupling having the value  $15.5\text{ meV}$ , accompanied by a weak ferromagnetic moment. The latter has been attributed to a small Dzyaloshinskii-Moriya interaction, of about  $1.1\text{ meV}$ . The experiment reported in Ref. 2 has found that the antiferromagnetic order of  $\text{LaTiO}_3$  has a G-type structure along the crystallographic  $a$  direction, while the ferromagnetic moment is along the  $c$  direction.

Because of the unusually small ordered moment, it has been proposed<sup>3</sup> that perhaps the cubic Kugel-Khomskii Hamiltonian<sup>4</sup> could be taken as a starting point for a successful interpretation of  $\text{LaTiO}_3$ . However, this cubic model has some very unusual symmetries which inhibit the appearance of long-range magnetic order at non-zero temperatures.<sup>5,6</sup> At strictly cubic symmetry, the fivefold degenerate  $d$ -levels on the Ti ions are split by the crystal field of the oxygen octahedra into the lower threefold degenerate  $t_{2g}$  levels, (occupied in Ti by a single electron) and the higher twofold degenerate  $e_g$  levels. In real materials, those degeneracies are frequently lifted by the Jahn-Teller distortion.

Figure 1 portrays the crystal structure of  $\text{LaTiO}_3$  (the enumeration we use for the Ti sites is marked in the figure). The unit cell contains four Ti ions, and the crystal has the symmetry of the space group  $Pbnm$ . The Jahn-Teller effect in  $\text{LaTiO}_3$  is caused by the twisting of the Ti-O bonds with respect to each other, i.e., by differ-

ences between the O-O bond lengths which amounts to a deviation of certain O-Ti-O bond angles away from  $90^\circ$ . The distortion leads to a crystal field that splits the levels,<sup>2</sup> yielding a crystal-field gap of about  $0.24\text{ eV}$  between the orbitally non-degenerate ground state and the first excited level, a value which has been confirmed by a study of photo-electron spectroscopy.<sup>7</sup> A comparison of the optical conductivity and of Raman data shows that the lowest orbital excitation is centered at about  $0.25\text{ eV}$ .<sup>8</sup> This value is in excellent agreement with the estimate of the crystal-field splitting according to Ref. 2. Furthermore, the non-degenerate ground-state orbital due to the crystal-field calculations given in Ref. 2 is consistent with the orbital order found in NMR measurements of the Ti- $3d$  quadrupole moment.<sup>9</sup> The presence of orbital order at low temperatures has also been inferred from measurements of the dielectric properties and the dynamical conductivity.<sup>10</sup>

An explanation of the magnetism of  $\text{LaTiO}_3$ , which is based on the crystal-field calculation given in Ref. 2, is presented in Ref. 11. The calculation included spin-orbit interaction on the Ti ions as well, and found accordingly that the superexchange coupling between neighboring Ti ions consists of the isotropic Heisenberg exchange, and the antisymmetric (Dzyaloshinskii-Moriya) and symmetric anisotropies, which appear as a result of the spin-orbit interaction. These anisotropies conspire together with the isotropic coupling to determine the magnetic order at low temperatures, shown in Fig. 2. By minimizing the magnetic energy of the classical ground state it was found<sup>11</sup> that the magnetic order of  $\text{LaTiO}_3$  is primarily that of a G-type antiferromagnet, with the ordered moment along the crystallographic  $a$  axis, accompanied by a weak ferromagnetic moment along the  $c$  axis, in good agreement with experiment. In addition, it was found that there is a small A-type moment of the spin compo-

nents along the  $b$  axis, which (although not yet detected in experiment) is allowed by the symmetry of the system.

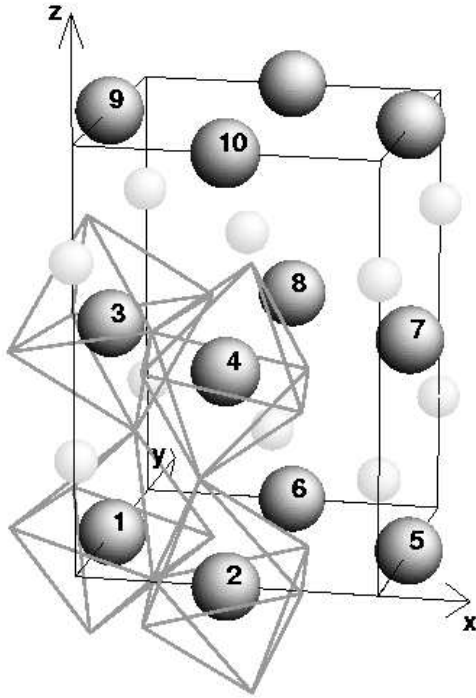


FIG. 1. The crystallographic structure of  $\text{LaTiO}_3$ . The ten Ti ions, which constitute the twelve inequivalent nearest-neighbor Ti-Ti bonds are enumerated. For simplicity, only the oxygen octahedra around the four crystallographically inequivalent Ti sites are shown. La ions from two layers are depicted as small spheres. We use orthorhombic coordinates, in which the  $x, y, z$  axes are oriented along the crystallographic  $a, b, c$  directions.

In this paper we calculate the spin-wave spectrum of  $\text{LaTiO}_3$ , which evolves from the magnetic ground state found in Ref. 11. Since the magnetic unit cell contains four sublattice magnetizations, the spin wave dispersion consists of four branches. In the zero spin-orbit coupling limit, these four branches collapse into two branches, an acoustic mode and an optical one, which both are two-fold degenerate. Accordingly, we term the two branches which evolve from the (zero spin-orbit coupling) acoustic waves as ‘acoustic modes’, and those which evolve from the optical ones as ‘optical modes’. At the Brillouin zone center, the energies of the two acoustic branches do not vanish but have gaps, of magnitudes 2.7 meV and 3.0 meV. These values are quite close to the zone-center gap of about 3.3 meV deduced from neutron scattering.<sup>1</sup> Furthermore, these two modes are approximately isotropic in the Brillouin zone, again in good agreement with the neutron scattering experiment.<sup>1</sup> We find that the two optical modes are quasi-degenerate, having a zone-center gap of about 43.3 meV. These modes have not been detected yet by neutron scattering but are

in good agreement with Raman data<sup>8</sup> where at low temperatures an excitation peak is seen, which is centered at about 40 meV and which disappears at  $T_N$ .

Our calculation employs linear spin-wave theory, which expresses the deviations of the spins from their ground state configuration in terms of Holstein-Primakoff bosons. We therefore begin our analysis by outlining in Sec. II the determination of that ground state configuration. We then continue to derive in Sec. III the spin-wave Hamiltonian, and to obtain the spin-wave dispersion. Section IV contains a numerical study of the dispersion curves, together with a detailed comparison with experiment. The summary of our results is presented in Sec. V.

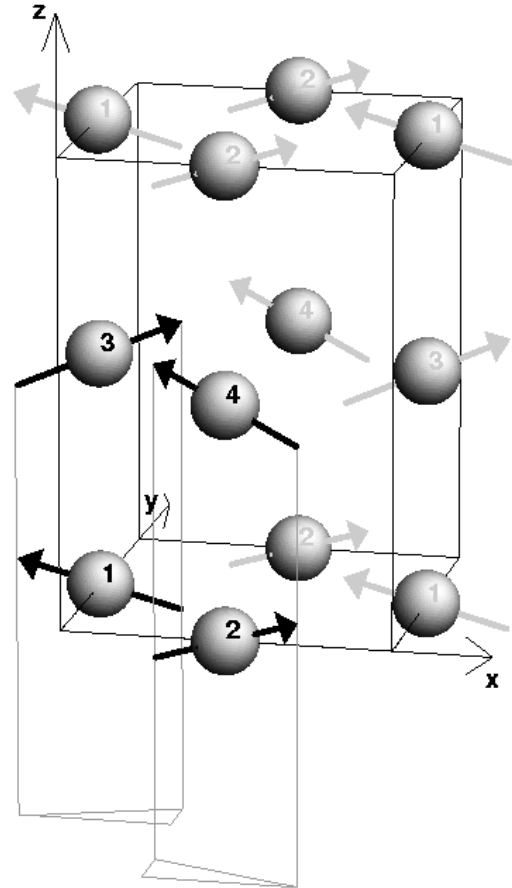


FIG. 2. The magnetic order of the Ti ions in the classical ground state of the effective spin Hamiltonian of the lattice. The ions are enumerated according to the sublattice to which they belong.

## II. THE MAGNETIC GROUND STATE

The analysis of the magnetic structure of  $\text{LaTiO}_3$ , carried out in Ref. 11, involves several steps. First, a microscopic Hamiltonian containing the relevant interactions on the Ti ions and between nearest-neighbor Ti ions is

derived. Treating this Hamiltonian in perturbation theory, one then derives the superexchange interactions between nearest-neighbor pairs of spins of the electrons in the ground-state orbitals. This effective spin Hamiltonian is summed over the entire Ti-lattice, to obtain the magnetic Hamiltonian. Finally, one minimizes the resulting magnetic energy of the system, to obtain the classical magnetic ground state. In this section we briefly review these steps.

The derivation of the microscopic Hamiltonian starts from a point-charge summation of the static crystal field for the Ti ions, employing a full Madelung sum over the crystal. This determines the eigenenergies and the eigenstates of the static crystal field acting on each Ti ion, i.e., the crystal-field  $d$  states. The effective hopping between the  $d$  orbitals of nearest-neighbor ions via the intervening oxygens is then written in terms of a Slater-Koster parametrization of the Ti-O hopping. The other interactions included in the microscopic Hamiltonian are the on-site Coulomb interaction and the on-site spin-orbit coupling on the Ti ions. In this way, the microscopic Hamiltonian pertaining to a pair of nearest-neighbor Ti ions (denoted  $m$  and  $n$ ) takes the form

$$H_{mn} = H_{mn}^0 + V_{mn}. \quad (1)$$

Here

$$H_{mn}^0 = H_{mn}^{\text{cf}} + H_{mn}^{\text{c}}, \quad (2)$$

where  $H^{\text{cf}}$  is the static crystal-field Hamiltonian, and  $H^{\text{c}}$  describes the intra-ionic Coulomb correlations of a doubly occupied  $d$ -shell. Because of the rather low symmetry of the system, in treating the  $\text{Ti}^{2+}$  ions which appear as intermediate states of the exchange processes it is necessary to take into account the full on-site Coulomb interaction matrix.<sup>11</sup> The other part of the Hamiltonian (1) is

$$V_{mn} = H_{mn}^{\text{tun}} + H_{mn}^{\text{so}}, \quad (3)$$

in which  $H^{\text{tun}}$  is the kinetic energy, described in terms of the effective hopping matrix, and  $H^{\text{so}}$  is the spin-orbit interaction. This part is treated in perturbation theory, in order to obtain from the Hamiltonian (1) an effective spin Hamiltonian, pertaining to the spins of the two Ti ions, which acts within the Hilbert space of the fourfold degenerate ground state of the unperturbed Hamiltonian  $H^0$ .

The detailed perturbation theory presented in Ref. 11, is carried out to second order in  $H^{\text{tun}}$  and up to second order in the spin-orbit coupling (scaled by the coupling strength  $\lambda$ ). This procedure yields a rich superexchange coupling between the spins of the non-degenerate crystal-field ground states of the  $\text{Ti}^{3+}$  ions. For a pair of two nearest-neighbor Ti ions, the effective single-bond spin Hamiltonian is found to be

$$h_{mn} = J_{mn} \mathbf{S}_m \cdot \mathbf{S}_n + \mathbf{D}_{mn} \cdot (\mathbf{S}_m \times \mathbf{S}_n) + \mathbf{S}_m \cdot \mathbf{A}_{mn}^s \cdot \mathbf{S}_n, \quad (4)$$

where  $J_{mn}$  is the isotropic Heisenberg coupling (second-order in the tunnelling amplitudes, and independent of  $\lambda$ ),  $\mathbf{D}_{mn}$  is the Moriya vector (second-order in the tunnelling amplitudes, and first order in  $\lambda$ ), and  $\mathbf{A}_{mn}^s$  is the symmetric anisotropy tensor (second-order in the tunnelling amplitudes and in  $\lambda$ ). As can be seen from Fig. 1, there are 12 inequivalent nearest-neighbor Ti-Ti bonds in the unit cell of  $\text{LaTiO}_3$ . By the symmetry operations of the space-group  $Pbnm$  the magnetic couplings of all 8 intra-plane bonds can be expressed in terms of those pertaining to the (12)-bond, and all 4 inter-plane ones in terms of those of the bond (13).<sup>11</sup> We list the numerical values of the couplings in Table I.<sup>12</sup> (The Tables are given on page 12.)

The magnetic Hamiltonian is found from the single-bond spin Hamiltonian (4), by summing over the entire Ti lattice. To this end, one decomposes the lattice into four sublattices, corresponding to the four inequivalent Ti sites of the unit cell (see Fig. 1). Although all four sublattice magnetizations are of equal magnitudes, their directions are all different. Denoting the sublattice magnetization per site by  $\mathbf{M}_i$ , the macroscopic magnetic Hamiltonian is found to be<sup>11</sup>

$$H_M = \sum_{ij} [I_{ij} \mathbf{M}_i \cdot \mathbf{M}_j + \mathbf{D}_{ij}^D \cdot (\mathbf{M}_i \times \mathbf{M}_j) + \mathbf{M}_i \cdot \mathbf{\Gamma}_{ij} \cdot \mathbf{M}_j], \quad (5)$$

where  $ij$  runs over the sublattice pairs (12), (13), (24), and (34) of Fig. 1. Here,  $I_{ij}$  are the macroscopic isotropic couplings,  $\mathbf{D}_{ij}^D$  are the Dzyaloshinskii vectors (to leading order in the spin-orbit coupling), which are the macroscopic antisymmetric anisotropies, and  $\mathbf{\Gamma}_{ij}$  are the macroscopic symmetric anisotropy tensors (of second order in the spin-orbit coupling). The relations between those macroscopic couplings and the microscopic single-bond couplings are listed in Table II, and the inter-relations between the macroscopic magnetic couplings of different bonds, which are dictated by the space group symmetries, are found in Table III.

The minimization of the magnetic Hamiltonian (5) yields the magnetic structure shown in Fig. 2. Table IV lists the details of this structure, in terms of the canting angles  $\varphi$  and  $\vartheta$  according to Ref. 11. This structure is going to be the basis for the spin-wave expansion carried out in the next section.

### III. THE SPIN-WAVE HAMILTONIAN

The deviations of the spins away from their directions in the classical ground state may be described in terms of Holstein-Primakoff boson operators. In our case, the system consists of four sublattices, which implies the introduction of four different bosonic fields, and, in turn, four branches in the spin-wave dispersion.

The first step in the standard calculation of spin-wave dispersions is the rotation of the local coordinates at each sublattice,  $i$ , such that the new  $z$  axis will point in the direction of the corresponding sublattice ground-state magnetization,  $\mathbf{M}_i$ . This rotation still leaves the freedom to choose the new local  $x$  and  $y$  axes, i.e., to rotate the new coordinate system around its  $z$  axis. Denoting the new local coordinate system by  $x'_i$ ,  $y'_i$  and  $z'_i$  ( $i = 1, 2, 3, 4$ ), we find that the convenient choice for our purposes (explained in Appendix A) is

$$\hat{z}'_i = \frac{\mathbf{M}_i}{M}, \quad \hat{y}'_i = \frac{\mathbf{M}_i \times \hat{x}}{m_i}, \quad \hat{x}'_i = \hat{y}'_i \times \hat{z}'_i, \\ M = |\mathbf{M}_i|, \quad m_i = \sqrt{(M_i^y)^2 + (M_i^z)^2}. \quad (6)$$

Consequently, there is a local rotation matrix  $U_i$ , pertaining to each of the four sublattices,

$$U_i = \begin{bmatrix} m_i & -M_i^y M_i^x / m_i & -M_i^z M_i^x / m_i \\ 0 & M_i^z / m_i & -M_i^y / m_i \\ M_i^x & M_i^y & M_i^z \end{bmatrix}, \quad (7)$$

which rotates the orthorhombic into the local coordinate system. We now apply this local rotation to the spin Hamiltonian (4), re-writing it for convenience in shorthand notation

$$h = \sum_{\langle mn \rangle} h_{mn} = \sum_{\langle mn \rangle} \mathbf{S}_m \cdot A_{mn} \cdot \mathbf{S}_n, \quad (8)$$

where  $A_{mn}$  is the  $3 \times 3$  superexchange matrix, comprising all three types of magnetic couplings. In the rotated coordinate system the spin Hamiltonian takes the form

$$h = \sum_{\langle mn \rangle} \mathbf{S}'_m \cdot A'_{mn} \cdot \mathbf{S}'_n, \quad (9)$$

where the primes denote the rotated quantities,

$$\mathbf{S}'_m = U_m \cdot \mathbf{S}_m, \quad A'_{mn} = U_m \cdot A_{mn} \cdot U_n^t. \quad (10)$$

We next introduce the Holstein-Primakoff boson fields<sup>13</sup> for each of the four sublattices. Since we consider only the Ti ions, it is convenient to use a coordinate system in which the Ti ions occupy the sites of a simple cubic lattice, of unit lattice constant (this picture is the appropriate one for comparing with the experimental spin-wave data,<sup>1</sup> as discussed in the next section). It is also convenient to use a coordinate system in which nearest-neighbor Ti ions are located along the axes (namely, to rotate the orthorhombic coordinates by  $-45^\circ$  around the  $z$  axis, see Fig. 2). Denoting the boson fields of sublattice 1, 2, 3, and 4 by  $a_{\mathbf{R}}$ ,  $b_{\mathbf{R}}$ ,  $c_{\mathbf{R}}$ , and  $d_{\mathbf{R}}$ , respectively, where  $\mathbf{R}$  is the radius vector to Ti No. 1 in Fig. 1, the spin-wave Hamiltonian, in the harmonic approximation takes the form

$$h_{\text{SW}} = h_{12}^{\text{sl}} + h_{34}^{\text{sl}} + h_{13}^{\text{sl}} + h_{24}^{\text{sl}}. \quad (11)$$

The first term here refers to the lower plane of the unit cell, the second to the upper plane, and the last two terms refer to the inter-plane couplings. Explicitly,

$$h_{12}^{\text{sl}} = \sum_{\mathbf{R}}' \{ [C_{12}(1) + C_{16}(1)] (a_{\mathbf{R}}^\dagger a_{\mathbf{R}} + b_{\mathbf{R}}^\dagger b_{\mathbf{R}}) \\ + a_{\mathbf{R}}^\dagger [C_{12}(2)(b_{\mathbf{R}} + b_{\mathbf{R}-2\mathbf{n}_x}) + C_{16}(2)(b_{\mathbf{R}-\mathbf{n}_x+\mathbf{n}_y} + b_{\mathbf{R}-\mathbf{n}_x-\mathbf{n}_y})] \\ + a_{\mathbf{R}}^\dagger [C_{12}(3)(b_{\mathbf{R}}^\dagger + b_{\mathbf{R}-2\mathbf{n}_x}^\dagger) + C_{16}(3)(b_{\mathbf{R}-\mathbf{n}_x+\mathbf{n}_y}^\dagger + b_{\mathbf{R}-\mathbf{n}_x-\mathbf{n}_y}^\dagger)] \} + \text{h. c.}, \\ h_{34}^{\text{sl}} = \sum_{\mathbf{R}}' \{ [C_{34}(1) + C_{38}(1)] (c_{\mathbf{R}}^\dagger c_{\mathbf{R}} + d_{\mathbf{R}}^\dagger d_{\mathbf{R}}) \\ + c_{\mathbf{R}}^\dagger [C_{34}(2)(d_{\mathbf{R}} + d_{\mathbf{R}-2\mathbf{n}_x}) + C_{38}(2)(d_{\mathbf{R}-\mathbf{n}_x+\mathbf{n}_y} + d_{\mathbf{R}-\mathbf{n}_x-\mathbf{n}_y})] \\ + c_{\mathbf{R}}^\dagger [C_{34}(3)(d_{\mathbf{R}}^\dagger + d_{\mathbf{R}-2\mathbf{n}_x}^\dagger) + C_{38}(3)(d_{\mathbf{R}-\mathbf{n}_x+\mathbf{n}_y}^\dagger + d_{\mathbf{R}-\mathbf{n}_x-\mathbf{n}_y}^\dagger)] \} + \text{h. c.}, \\ h_{13}^{\text{sl}} = \sum_{\mathbf{R}}' \{ C_{13}(1)(a_{\mathbf{R}}^\dagger a_{\mathbf{R}} + c_{\mathbf{R}}^\dagger c_{\mathbf{R}}) \\ + C_{13}(2)a_{\mathbf{R}}^\dagger (c_{\mathbf{R}} + c_{\mathbf{R}-2\mathbf{n}_z}) + C_{13}(3)a_{\mathbf{R}}^\dagger (c_{\mathbf{R}}^\dagger + c_{\mathbf{R}-2\mathbf{n}_z}^\dagger) \} + \text{h. c.}, \\ h_{24}^{\text{sl}} = \sum_{\mathbf{R}}' \{ C_{24}(1)(b_{\mathbf{R}}^\dagger b_{\mathbf{R}} + d_{\mathbf{R}}^\dagger d_{\mathbf{R}}) \\ + C_{24}(2)b_{\mathbf{R}}^\dagger (d_{\mathbf{R}} + d_{\mathbf{R}-2\mathbf{n}_z}) + C_{24}(3)b_{\mathbf{R}}^\dagger (d_{\mathbf{R}}^\dagger + d_{\mathbf{R}-2\mathbf{n}_z}^\dagger) \} + \text{h. c.} \quad (12)$$

Here  $\mathbf{n}_\alpha$  is a unit vector along the  $\alpha$ -direction, where  $\alpha = x, y, z$ , and the Ti ion marked by 1 in Fig. 1 is at the origin. The summations then extend only over the Ti ions No. 1 in each unit cell (this is indicated by the prime on the summation symbols). The coupling coefficients  $C_{mn}(\ell)$  in Eq. (12) are given by combinations of the superexchange matrix elements  $(A'_{mn})^{\alpha\beta}$ ,

$$C_{mn}(1) = -\frac{1}{2}(A'_{mn})^{zz}, \\ C_{mn}(2) = \frac{1}{4}[(A'_{mn})^{xx} + (A'_{mn})^{yy} + i((A'_{mn})^{yx} - (A'_{mn})^{xy})], \\ C_{mn}(3) = \frac{1}{4}[(A'_{mn})^{xx} - (A'_{mn})^{yy} + i((A'_{mn})^{yx} + (A'_{mn})^{xy})]. \quad (13)$$

In writing down Eq. (12), we have omitted constant terms. The transformation to the Holstein-Primakoff operators

yields also terms which are linear in the boson fields; these vanish upon summing over all bonds (see Appendix A) due to the proper choice of the local coordinate system.

Our magnetic unit cell is spanned by the vectors  $(1, 1, 0)$ ,  $(1, -1, 0)$ , and  $(0, 0, 2)$ , and the corresponding magnetic Brillouin zone (MBZ) is defined by

$$|q_x + q_y| \leq \pi, \quad |q_z| \leq \frac{\pi}{2}. \quad (14)$$

By introducing the Fourier transforms of the operators,

$$\begin{aligned} a_{\mathbf{R}}^\dagger &= \sqrt{\frac{1}{N}} \sum_{\mathbf{q} \in \text{MBZ}} e^{i\mathbf{q}\mathbf{R}} a_{\mathbf{q}}^\dagger, & b_{\mathbf{R}}^\dagger &= \sqrt{\frac{1}{N}} \sum_{\mathbf{q} \in \text{MBZ}} e^{i\mathbf{q}(\mathbf{R}+\mathbf{n}_x)} b_{\mathbf{q}}^\dagger, \\ c_{\mathbf{R}}^\dagger &= \sqrt{\frac{1}{N}} \sum_{\mathbf{q} \in \text{MBZ}} e^{i\mathbf{q}(\mathbf{R}+\mathbf{n}_z)} c_{\mathbf{q}}^\dagger, & d_{\mathbf{R}}^\dagger &= \sqrt{\frac{1}{N}} \sum_{\mathbf{q} \in \text{MBZ}} e^{i\mathbf{q}(\mathbf{R}+\mathbf{n}_x+\mathbf{n}_z)} d_{\mathbf{q}}^\dagger, \end{aligned} \quad (15)$$

where  $N$  is the total number of magnetic unit cells, the spin-wave Hamiltonian (11) becomes

$$h_{\text{SW}} = \sum_{\mathbf{q}} h_{\text{SW}}(\mathbf{q}), \quad (16)$$

where

$$\begin{aligned} h_{\text{SW}}(\mathbf{q}) &= C_1 \left( a_{\mathbf{q}}^\dagger a_{\mathbf{q}} + b_{\mathbf{q}}^\dagger b_{\mathbf{q}} + c_{\mathbf{q}}^\dagger c_{\mathbf{q}} + d_{\mathbf{q}}^\dagger d_{\mathbf{q}} \right) \\ &+ \left[ C_2^\parallel (\cos q_x + \cos q_y) (a_{\mathbf{q}}^\dagger b_{\mathbf{q}} + c_{\mathbf{q}}^\dagger d_{\mathbf{q}}) + \text{h. c.} \right] + \left[ C_2^\perp \cos q_z (a_{\mathbf{q}}^\dagger c_{\mathbf{q}} + b_{\mathbf{q}}^\dagger d_{\mathbf{q}}) + \text{h. c.} \right] \\ &+ \left[ (C_3^\parallel \cos q_x + C_3^{*\parallel} \cos q_y) (a_{\mathbf{q}}^\dagger b_{-\mathbf{q}}^\dagger + c_{\mathbf{q}}^\dagger d_{-\mathbf{q}}^\dagger) + \text{h. c.} \right] + \left[ C_3^\perp \cos q_z a_{\mathbf{q}}^\dagger c_{-\mathbf{q}}^\dagger + C_3^{*\perp} \cos q_z b_{\mathbf{q}}^\dagger d_{-\mathbf{q}}^\dagger + \text{h. c.} \right]. \end{aligned} \quad (17)$$

The coefficients appearing in this equation are linear combinations of the previous coefficients  $C_{mn}(\ell)$  (see Appendix A),

$$C_1 = 2C_{13}(1) + 4C_{12}(1) = C_1^*, \quad C_2^\perp = 2C_{13}(2) = C_2^{\perp*}, \quad C_2^\parallel = 2C_{12}(2), \quad C_3^\perp = 2C_{13}(3), \quad C_3^\parallel = 2C_{12}(3). \quad (18)$$

These are related to the original spin-coupling coefficients of Eq. (4), but are not reproduced here explicitly, since their expressions are very long.

The spin-wave dispersion pertaining to the Hamiltonian (16) is calculated in Appendix B, leading to the result

$$\begin{aligned} \Omega_1^2(\mathbf{q}) &= (C_1 - C_2^\perp \cos q_z)^2 - |C_3^\perp|^2 \cos^2 q_z + |C_2^\parallel|^2 (\cos q_x + \cos q_y)^2 \\ &\quad - |C_3^\parallel \cos q_x + C_3^{*\parallel} \cos q_y|^2 - (\cos q_x + \cos q_y) W(\cos q_z), \\ \Omega_2^2(\mathbf{q}) &= \Omega_1^2(\mathbf{q} + \mathbf{Q}), \quad \text{with } \mathbf{Q} = (0, 0, \pi), \\ \Omega_3^2(\mathbf{q}) &= \Omega_1^2(\mathbf{q} + \mathbf{Q}'), \quad \text{with } \mathbf{Q}' = (\pi, \pi, 0), \\ \Omega_4^2(\mathbf{q}) &= \Omega_1^2(\mathbf{q} + \mathbf{Q}''), \quad \text{with } \mathbf{Q}'' = \mathbf{Q} + \mathbf{Q}' = (\pi, \pi, \pi), \end{aligned} \quad (19)$$

where

$$\begin{aligned} W^2(\cos q_z) &= 4 \left[ (C_1 - C_2^\perp \cos q_z)^2 - |C_3^\perp|^2 \cos^2 q_z \right] \left[ |C_2^\parallel|^2 - \left( \frac{C_3^\parallel + C_3^{*\parallel}}{2} \right)^2 \right] \\ &\quad + \left[ (C_3^{\perp*} C_2^\parallel + C_3^\perp C_2^{*\parallel}) \cos q_z + (C_1 - C_2^\perp \cos q_z) (C_3^\parallel + C_3^{*\parallel}) \right]^2. \end{aligned} \quad (20)$$

Each of the branches has tetragonal symmetry, i.e.,  $\Omega_i(q_x, q_y, q_z) = \Omega_i(q_y, q_x, q_z) = \Omega_i(-q_x, q_y, q_z) = \Omega_i(q_x, -q_y, q_z) = \Omega_i(q_x, q_y, -q_z)$ .

Equations (19) contain our final result for the spin-wave spectrum of  $\text{LaTiO}_3$ . Evidently, the details of the

spectrum can be obtained only numerically: One has to write the spin-wave coefficients, Eqs. (18), in terms of those appearing in Eqs. (13), and express the latter via Eqs. (8) and (10) in terms of the original coefficients of the spin Hamiltonian (4) using the values listed in Table

I. These results are then used in constructing the dispersion. We carry out this procedure in the next section, confining ourselves to the wave vectors explored in the neutron scattering and Raman experiments, respectively.

When the spin-orbit coupling  $\lambda$  is set to zero, the coefficients appearing in Eqs. (19) simplify to

$$\begin{aligned} C_1 &= 2J_{12} + J_{13}, & C_2^\perp &= C_2^\parallel = 0, \\ C_3^\perp &= -J_{13}, & C_3^\parallel &= -J_{12}, \end{aligned} \quad (21)$$

where  $J_{12}$  is the isotropic in-plane Heisenberg coupling, and  $J_{13}$  is the Heisenberg coupling between planes. In that case [note that  $\cos q_z = |\cos q_z|$  in the Brillouin zone, see Eq. (14)]

$$\begin{aligned} \Omega_1^2(\mathbf{q}) &= \Omega_2^2(\mathbf{q}) = (2J_{12} + J_{13})^2 \\ &- (J_{12}(\cos q_x + \cos q_y) + J_{13}|\cos q_z|)^2, \end{aligned} \quad (22)$$

while the expression for  $\Omega_3^2(\mathbf{q}) = \Omega_4^2(\mathbf{q})$  is obtained upon changing  $\cos q_x + \cos q_y$  to  $-\cos q_x - \cos q_y$ . At the zone center  $\Omega_1$  and  $\Omega_2$  vanish, while  $\Omega_3$  and  $\Omega_4$  have a gap equal to  $\sqrt{8J_{12}J_{13}}$ . Obviously, in the absence of spin-orbit coupling the magnetic unit cell includes only two sublattices (in that case, sublattice 1 and sublattice 4 can be combined into one sublattice, and so can sublattice 2 and sublattice 3 in Fig. 2). The Brillouin zone corresponding to this smaller magnetic cell is twice as large as the one of Eq. (14). By “folding out” the optical mode into this larger Brillouin zone, one reproduces the usual gap-less dispersion of the pure Heisenberg model. At finite values of the spin-orbit coupling all modes have gaps at the zone center, but those of  $\Omega_1$  and  $\Omega_2$  are much smaller than the ones of the other two modes. For this reason, we term the  $\Omega_1(\mathbf{q})$  and the  $\Omega_2(\mathbf{q})$  branches ‘acoustic modes’ and  $\Omega_3(\mathbf{q})$  and  $\Omega_4(\mathbf{q})$  are referred to as optical modes. Optical spin-wave modes have been detected, for instance, in bilayer cuprates.<sup>14–16</sup>

#### IV. NUMERICAL RESULTS FOR THE SPIN-WAVE DISPERSION

For the model parameters we use, it turns out that the two acoustic branches as well as the two optical branches are nearly degenerate. The reason is the smallness of the angle  $\varphi$ , which leads to an additional translational symmetry which is nearly fulfilled by the classical ground state. This “quasi”-symmetry corresponds to the translation by the vector  $\mathbf{R}_{14}$  which connects the Ti ions No. 1 and 4 (see Figs. 1 and 2). For  $\varphi=0$  this symmetry is exact, and the magnetic unit cell contains only two ions. In that case the spin-wave dispersion consists of two branches. As we have a small deviation from this ideal case, we obtain two pairs of quasi-degenerate branches.

#### A. Comparison of the acoustic branches with neutron scattering data

We begin our discussion here by recalling the experimental results of Ref. 1. The authors of Ref. 1 have fitted their neutron scattering data with an isotropic single-branch spectrum parametrized as

$$\Omega(\mathbf{q}) \simeq J \sqrt{\left(3 + \frac{\Delta^2}{6J^2}\right)^2 - (\cos q_x + \cos q_y + \cos q_z)^2}. \quad (23)$$

This assumes an isotropic Heisenberg coupling,  $J$ , for the entire Ti lattice, namely, the same coupling for the bond (12) and the bond (13) of Fig. 1, and introduces a zone-center spin-wave gap,  $\Delta$ . The experimentally determined values of these parameters are

$$J = 15.5 \pm 1.0 \text{ meV}, \quad \Delta = 3.3 \pm 0.3 \text{ meV}. \quad (24)$$

In the following, we compare the fitted function, Eq. (23), with the acoustic branches  $\Omega_1(\mathbf{q})$  and  $\Omega_2(\mathbf{q})$ .

Although the symmetry of our spin-wave Hamiltonian allows for two acoustic modes, the resolution of the dispersion measurements, which amounts to about 10 % at any given point  $\mathbf{q}$  in the Brillouin zone,<sup>17</sup> is insufficient to resolve the two branches. To demonstrate this point, and to compare in detail the experimental findings with our expressions, we proceed as follows. Firstly, we average the Heisenberg couplings pertaining to the different bonds (calculated in Ref. 11) over the six Ti-Ti bonds in which each Ti ion is participating,

$$\frac{4J_{12} + 2J_{13}}{6} = 15.89 \text{ meV}. \quad (25)$$

Clearly this value agrees with the experimental one given in Eq. (24), within the accuracy of the experiment. Secondly, we calculate the zone-center gaps as found from our calculation. Following the numerical procedure outlined at the end of the previous section, we find

$$\begin{aligned} \Delta_1 &= \Omega_1(\mathbf{0}) = 2.71 \text{ meV}, \\ \Delta_2 &= \Omega_2(\mathbf{0}) = 2.98 \text{ meV}. \end{aligned} \quad (26)$$

We have found that the splitting between the two calculated acoustic branches reaches its maximum at the zone center, where

$$\frac{\Delta_1}{\Delta_2} = 91.14 \%. \quad (27)$$

This discrepancy is within the uncertainty of about 10 % of the measured spin-wave energies of Ref. 1.

Away from the zone center the two acoustic branches are quasi-degenerate. We estimate the tetragonal anisotropy of the dispersion by comparing the dispersions at wave vectors  $\mathbf{q} = (\pi/2, 0, 0)$  and  $\mathbf{q} = (0, 0, \pi/2)$ ,

$$\frac{\Omega_1(0, 0, \frac{\pi}{2})}{\Omega_1(\frac{\pi}{2}, 0, 0)} = 91.34 \%, \quad \frac{\Omega_2(0, 0, \frac{\pi}{2})}{\Omega_2(\frac{\pi}{2}, 0, 0)} = 91.29 \%. \quad (28)$$

This implies that the tetragonal anisotropy is also less than the uncertainty of the measured spin-wave energies. The calculated dispersions along selected directions in the Brillouin zone are depicted in Figs. 3, together with the optical branches which we will discuss in Sec. IV B and the experimental dispersion computed from Eq. (23). The agreement between the acoustic branches and the experimental dispersion is satisfying.

It is harder to infer the experimentally quoted value<sup>1</sup> of the Dzyaloshinskii-Moriya interaction, 1.1 meV, (which does not agree well with our values for the Dzyaloshinskii vectors, see Table I), from the calculated dispersion. We therefore attempt to estimate the effects of the two types of anisotropies, antisymmetric and symmetric, on the spin-wave dispersion by analyzing two cases: (i) Switching off all antisymmetric anisotropies,  $\mathbf{D}_{mn} = \mathbf{0}$ , (all other terms are accounted for according to their calculated values, see Table I) and (ii) switching off all symmetric anisotropies,  $A_{mn}^s = 0$ , while keeping the contributions of the antisymmetric ones. In both cases we examine the spin canting, i.e., the ground-state configuration of the magnetization, and the zone-center gap of the dispersion. (The dispersion away from the zone center is dominated by the Heisenberg couplings.)

(i) In the absence of the Dzyaloshinskii-Moriya interaction, the canting practically disappears. We find that the canting angles almost vanish,

$$\varphi = -0.04^\circ, \vartheta = 0.00^\circ, \text{ if } \mathbf{D}_{mn} = \mathbf{0}. \quad (29)$$

However, the zone-center gap is enhanced compared to its actual values, Eq. (26),

$$\Delta_1 = \Delta_2 = 4.73 \text{ meV}, \text{ if } \mathbf{D}_{mn} = \mathbf{0}. \quad (30)$$

(ii) In the absence of the symmetric anisotropies the spin canting is almost the same as given in Table IV,

$$\varphi = 1.47^\circ, \vartheta = 0.80^\circ, \text{ if } A_{mn}^s = 0. \quad (31)$$

Switching off continuously the symmetric anisotropies, we find that the zone-center gap first closes and then even becomes imaginary as the symmetric anisotropies approach zero. This unphysical result shows that one is not allowed to consider only the antisymmetric anisotropies resulting from the spin-orbit interaction, without including the symmetric ones as well. Indeed, as has been already pointed out in Refs. 18 and 19, a systematic treatment of the effect of the spin-orbit interaction on the spin couplings must include both anisotropies. They both contribute to the magnetic energy terms of the same order in the spin-orbit coupling parameter.

Comparing these two fictitious cases, we conclude that the spin-canting is dominated by the antisymmetric anisotropies, while the zone-center gap of the dispersion is governed by the symmetric anisotropies. It is therefore a somewhat questionable procedure to deduce the antisymmetric anisotropy of the spin coupling from the spin-wave dispersion, taking into account only the Moriya vectors, as has been done in Ref. 1. This is again related to

the fact that both the Dzyaloshinskii-Moriya interactions and the symmetric anisotropies induced by the spin-orbit coupling appear in the same order in the magnetic energy and in the spin-wave dispersion.<sup>20</sup>

The manner by which the various anisotropic spin couplings, in a low-symmetry system like LaTiO<sub>3</sub>, can be deduced from an experimentally obtained spin-wave spectrum therefore remains unsettled. In our case, the spin-wave Hamiltonian, Eq. (17), depends on 8 parameters [note that some of the coefficients, Eqs. (18), are complex]. Furthermore, even the knowledge of these 8 parameters does not suffice in our case to trace backwards the parameters of the spin Hamiltonian, Eq. (4). The reason being that the coefficients involving the matrix elements  $(A'_{mn})^{xz}$  and  $(A'_{mn})^{yz}$  [see Eq. (13)] disappear altogether from the spin-wave Hamiltonian (see Appendix A). The conclusion is that it is possible to use certain numerical values for the various types of spin couplings and to investigate their consistency with the experimentally detected spin-wave dispersion (as done above). However, an unequivocal deduction of spin-coupling parameters from spin-wave spectra is not possible due to the low symmetry of this system.

## B. The optical branches

The two calculated optical branches, depicted in Figs. 3, are practically indistinguishable in the entire Brillouin zone. Their zone-center gaps are

$$\begin{aligned} \Delta_3 &= \Omega_3(\mathbf{0}) = 43.32 \text{ meV}, \\ \Delta_4 &= \Omega_4(\mathbf{0}) = 43.34 \text{ meV}. \end{aligned} \quad (32)$$

So far, branches with such a large zone-center gap have not been detected by neutron scattering.<sup>1</sup> Possible reasons are: (i) The signal in the energy range of the optical branches has a rather low intensity (as compared to the lower energy regions); (ii) The spin-wave signal in this energy range is accompanied, and possibly is hidden, by phonon excitations.<sup>17</sup> However, despite of these two problems, in principle it might be possible to detect the dispersion of the optical branches by neutron scattering.<sup>17</sup> Our prediction is that the dispersion of the optical modes will be qualitatively different from that of the acoustic ones. These modes will not have the approximate isotropy of the acoustic modes, but will show a larger tetragonal anisotropy. We find

$$\frac{\Omega_3(0,0,\frac{\pi}{2})}{\Omega_3(\frac{\pi}{2},0,0)} = 70.47\%, \quad \frac{\Omega_4(0,0,\frac{\pi}{2})}{\Omega_4(\frac{\pi}{2},0,0)} = 70.44\%. \quad (33)$$

These relations can serve as a further check of our model.

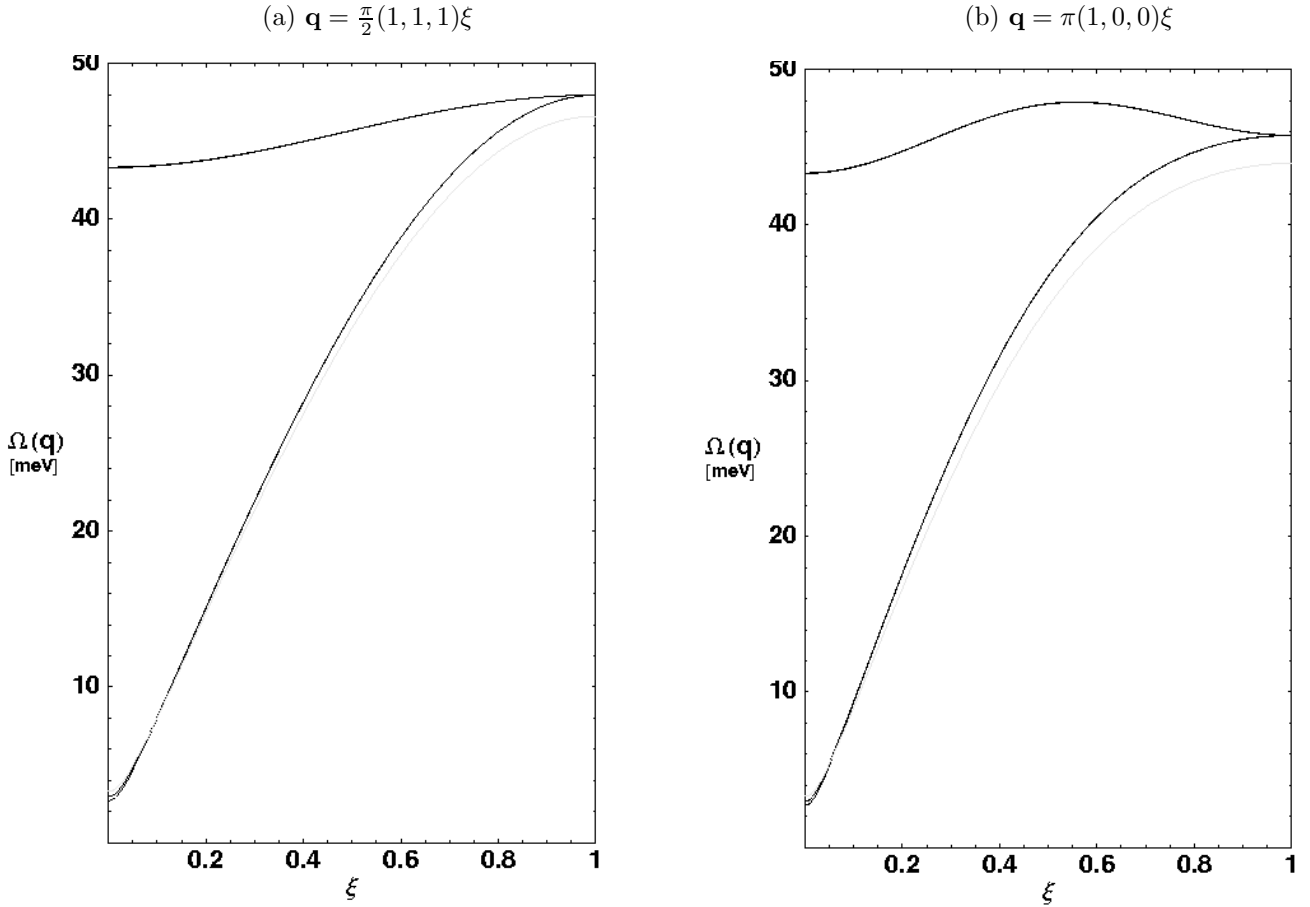
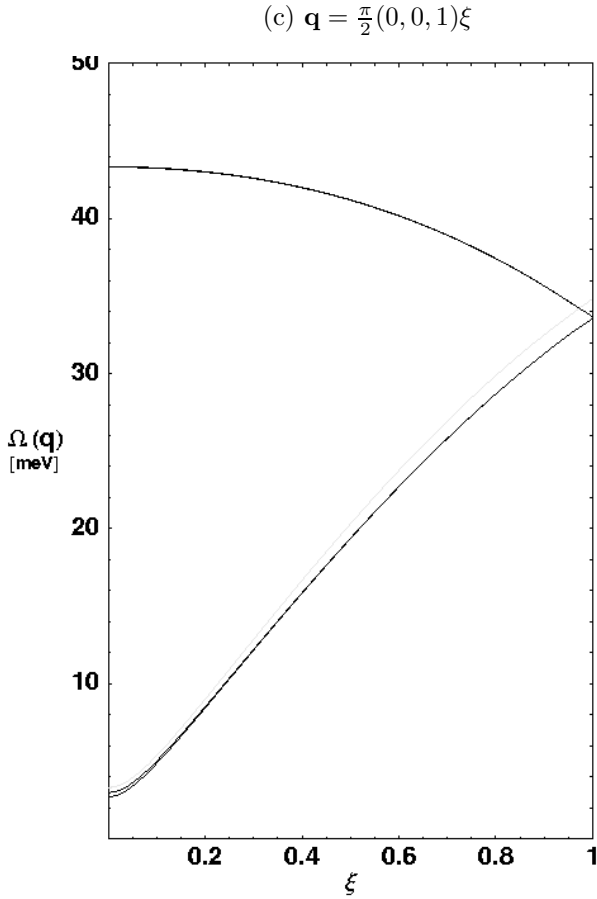


FIG. 3. The spin-wave dispersion along selected directions in the magnetic Brillouin zone. We use pseudo-cubic coordinates, in which the Ti ions No. 1 and 2 are located along the  $x$  axis. Panels (a)–(c) show (in black) the four branches  $\Omega_i(\mathbf{q})$  of the calculated dispersion and (in grey) the single branch  $\Omega(\mathbf{q})$  which has been fitted onto neutron scattering experiments, Eq. (23). The acoustic branches  $\Omega_1(\mathbf{q})$  and  $\Omega_2(\mathbf{q})$  are quasi-degenerate, such that away from the zone center no splitting between them can be seen. The optical branches  $\Omega_3(\mathbf{q})$  and  $\Omega_4(\mathbf{q})$  are practically indistinguishable over the entire Brillouin zone. (a) The dispersion along  $(1,1,1)$ . This direction is chosen because the experimental paper on the neutron scattering contains a plot along this direction where the measured points of the dispersion are shown.<sup>1</sup> Though the calculated acoustic branches of the dispersion give slightly lower energies at the zone-center than the fitted function and slightly higher energies at the zone edge, these deviations are within the uncertainty of the measurement and hence, the agreement of our calculated dispersion with the the measured points and with the fitted function is satisfying. The splitting of the calculated acoustic branches at the zone center is too small to be resolved in the experiment. From panels (b) and (c) one can see that the tetragonal anisotropy of the calculated acoustic branches is rather small. The agreement between the acoustic branches and the neutron scattering data is satisfying also along the  $(1,0,0)$  [panel (b)] and  $(0,0,1)$  [panel(c)] directions.

In contrast to the absence of experimental evidence for the optical modes in the neutron scattering experiment, Raman spectroscopy<sup>8</sup> at low temperatures does show a pronounced peak centered at about 40 meV. This energy is consistent with our calculated optical branches  $\Omega_3(\mathbf{q})$  and  $\Omega_4(\mathbf{q})$ . In Raman spectroscopy only the zero wave vector excitation of the optical branches can be observed. In principle, Raman spectroscopy is only sensitive to  $S_z=0$  excitations but this selection rule can be broken by the spin-orbit coupling. The Raman peak disappears at the Néel temperature, giving evidence for a magnetic origin. Studying spin-wave energies in Raman spectroscopy might be subject to similar difficulties as neutron scattering when it comes to the phonons' role. Since the pronounced peak at about 40 meV has a very large intensity, its explanation may well have to include the coupling to lattice modes, in addition to the optical spin-wave modes.





## V. SUMMARY

We have presented a detailed analysis of the spin-wave spectrum in  $\text{LaTiO}_3$ . We have found that the spin-wave spectrum of this system consists of two pairs of quasi-degenerate branches. The modes belonging to one of the pairs have a rather small zone-center gap, about 3 meV,

## APPENDIX A: THE CHOICE OF THE ROTATION MATRIX

As is mentioned in the text, the local coordinate system given in Eq. (6), in which the local  $z$  axis points along the direction of the moment in the classical ground state is still ambiguous in that it can be rotated arbitrarily around its  $z$ -axis. Here we show that our choice, Eqs. (6) and (7), leads to a considerable simplification in the calculation of the spin-wave Hamiltonian.

Let us suppose that the local coordinate system of Eq. (6) at each of the four lattices sites is further rotated around its local  $z$ -axis by an angle  $\rho_i$ , ( $i = 1, 2, 3, 4$ ). The rotation matrices  $U_i$  of Eq. (7) are then replaced by

and are approximately isotropic over the Brillouin zone. The dispersion and the gap of these two modes are shown to reproduce the experimental data of the neutron scattering experiment carried out on  $\text{LaTiO}_3$ .<sup>1</sup> The quasi-degenerate modes belonging to the second pair have a large zone-center gap, about 43 meV, and their dispersion shows sizeable tetragonal anisotropy in the Brillouin zone. While not yet detected in neutron scattering experiments, (perhaps for technical reasons as indicated above), the zone-center gap of these modes is consistent with Raman data.<sup>8</sup>

Our spin-wave dispersion is calculated on the basis of the detailed low-temperature magnetic structure of  $\text{LaTiO}_3$ , which we have analyzed in a previous paper.<sup>11</sup> There, we have used the experimentally verified orbital ordering in this system, to develop the superexchange interaction between nearest-neighbor Ti ions. As detailed in Ref. 11, and summarized in the Introduction section above, the complicated magnetic structure that we have obtained, which involves a predominant G-type antiferromagnetic order along the  $a$  axis and a canted ferromagnetic one along the  $c$  axis, agrees beautifully with all available experimental findings. In view of the good agreement we have found in the present study with the neutron and Raman scattering data, it might be concluded that our analysis has yielded a detailed understanding of the magnetism in  $\text{LaTiO}_3$ . In addition, we have indicated above a rather detailed prediction regarding the behavior of the higher-energy modes. We hope that these will be studied experimentally, and will be compared with our calculations.

## ACKNOWLEDGMENTS

We gratefully acknowledge discussions with M. Grüninger and B. Keimer. This work was partially supported by the German-Israeli Foundation for Research (GIF), and by the US-Israel Binational Science Foundation (BSF).

$$U_{i\rho_i} = U_i \cdot \begin{bmatrix} \cos \rho_i & -\sin \rho_i & 0 \\ \sin \rho_i & \cos \rho_i & 0 \\ 0 & 0 & 1 \end{bmatrix}, \quad (\text{A1})$$

and the corresponding superexchange matrices, Eq. (10), are transformed accordingly as

$$A'_{mn\rho_m\rho_n} = U_{m\rho_m}^t \cdot A'_{mn} \cdot U_{n\rho_n}, \quad (\text{A2})$$

where

$$A'_{mn00} \equiv A'_{mn} \quad (\text{A3})$$

is the superexchange matrix of Eq. (10).

The arbitrary rotations described above will modify the coefficients  $C_{mn}(\ell)$ , Eqs. (13), appearing in the spin-wave Hamiltonian. Denoting these modified coefficients

by  $C_{mn\rho_m\rho_n}(\ell)$ , such that  $C_{mn00}(\ell) \equiv C_{mn}(\ell)$ , we find in Table III the following inter-relations (using the symmetries listed

$$\begin{aligned}
C_{12\rho_1\rho_2}(1) &= C_{34\rho_3\rho_4}(1) = C_{16\rho_1\rho_2}(1) = C_{38\rho_3\rho_4}(1) = C_{12}(1) = C_{12}^*(1), \\
C_{13\rho_1\rho_3}(1) &= C_{24\rho_2\rho_4}(1) = C_{13}(1) = C_{13}^*(1), \\
C_{12[16]\rho_1\rho_2}(2) &= C_{12[16]}(2)e^{i(\rho_2-\rho_1)}, \quad C_{34[38]\rho_3\rho_4}(2) = C_{34[38]}(2)e^{i(\rho_4-\rho_3)}, \\
C_{12\rho_1\rho_2}(2) &= C_{16\rho_1\rho_2}(2) = C_{34\rho_3\rho_4}(2) = C_{38\rho_3\rho_4}(2) \text{ if } \rho_4 - \rho_3 = \rho_2 - \rho_1, \\
C_{13\rho_1\rho_3}(2) &= C_{24\rho_2\rho_4}(2) = C_{13}(2) = C_{13}^*(2) \\
C_{12[16]\rho_1\rho_2}(3) &= C_{12[16]}(3)e^{-i(\rho_1+\rho_2)}, \quad C_{34[38]\rho_3\rho_4}(3) = C_{34[38]}(3)e^{-i(\rho_3+\rho_4)} \\
C_{12\rho_1\rho_2}(3) &= C_{16\rho_1\rho_2}^*(3) = C_{34\rho_3\rho_4}(3) = C_{38\rho_3\rho_4}^*(3) \text{ if } \rho_1 + \rho_2 = \rho_3 + \rho_4, \\
C_{13\rho_1\rho_3}(3) &= C_{13}(3)e^{-i(\rho_1+\rho_3)}, \quad C_{24\rho_2\rho_4}(3) = C_{24}(3)e^{-i(\rho_2+\rho_4)}, \quad C_{13}(3) = C_{24}^*(3).
\end{aligned} \tag{A4}$$

It is thus seen that with the choice employed in Eq. (6), namely  $\rho_i = 0$  ( $i = 1, 2, 3, 4$ ), the following relations are obtained

$$\begin{aligned}
C_{12}(1) &= C_{16}(1) = C_{34}(1) = C_{38}(1), \quad C_{13}(1) = C_{24}(1), \quad 2C_{12}(1) + C_{13}(1) \equiv \frac{1}{2}C_1, \\
C_{12}(2) &= C_{16}(2) = C_{34}(2) = C_{38}(2) \equiv \frac{1}{2}C_2^\parallel, \quad C_{13}(2) = C_{24}(2) \equiv \frac{1}{2}C_2^\perp = \frac{1}{2}C_2^{\perp*} \\
C_{12}(3) &= C_{34}(3) = C_{16}^*(3) = C_{38}^*(3) \equiv \frac{1}{2}C_3^\parallel, \quad C_{13}(3) = C_{24}^*(3) \equiv \frac{1}{2}C_3^\perp.
\end{aligned} \tag{A5}$$

Here we have introduced the coefficients  $C_1$ ,  $C_2^{\parallel,\perp}$ , and  $C_3^{\parallel,\perp}$  that are used in our spin-wave Hamiltonian, Eq. (17).

As is mentioned in the text, the Holstein-Primakoff transformation gives rise to terms linear in the boson operators. The coefficients of these terms are

$$C_{mn}(4) = \frac{1}{4}((A'_{mn})^{xz} + i(A'_{mn})^{yz}). \tag{A6}$$

When summed over all single-bond contributions, these coefficients vanish. For example, the absolute value of the coefficient of the boson operator  $a_{\mathbf{R}}^\dagger$  is

$$2|C_{12}(4) + C_{16}(4) + C_{13}(4)| = \frac{1}{2}\sqrt{[A'_{12}{}^{xz} + A'_{16}{}^{xz} + A'_{13}{}^{xz}]^2 + [A'_{12}{}^{yz} + A'_{16}{}^{yz} + A'_{13}{}^{yz}]^2} = 0. \tag{A7}$$

Employing Eqs. (10), we have written each of the terms appearing in the square root explicitly, and verified that they both vanish. A similar argument prevails for the other coefficients of the linear terms.

## APPENDIX B: THE SPIN-WAVE DISPERSION

In order to obtain the spin-wave dispersion resulting from the Hamiltonian (17), it is convenient to first introduce a short-hand notation for this Hamiltonian. To this end we write

$$h_{\text{SW}}(\mathbf{q}) = \sum_{\mu\nu} \left( \mathcal{H}_{\mu\nu}^a(\mathbf{q}) \xi_\mu^\dagger(\mathbf{q}) \xi_\nu(\mathbf{q}) + \frac{1}{2} \mathcal{H}_{\mu\nu}^b(\mathbf{q}) \xi_\mu^\dagger(\mathbf{q}) \xi_\nu^\dagger(-\mathbf{q}) + \frac{1}{2} \mathcal{H}_{\mu\nu}^{b*}(\mathbf{q}) \xi_\mu(\mathbf{q}) \xi_\nu(-\mathbf{q}) \right), \tag{B1}$$

where

$$\boldsymbol{\xi}(\mathbf{q}) = \begin{bmatrix} a_{\mathbf{q}} \\ b_{\mathbf{q}} \\ c_{\mathbf{q}} \\ d_{\mathbf{q}} \end{bmatrix}, \quad \boldsymbol{\xi}^\dagger(\mathbf{q}) = [a_{\mathbf{q}}^\dagger, b_{\mathbf{q}}^\dagger, c_{\mathbf{q}}^\dagger, d_{\mathbf{q}}^\dagger], \tag{B2}$$

and the Hamiltonian matrices are conveniently written in the form

$$\mathcal{H}^a(\mathbf{q}) = \begin{bmatrix} \mathcal{H}_1 & \mathcal{H}_2 \\ \mathcal{H}_2 & \mathcal{H}_1 \end{bmatrix}, \quad \mathcal{H}_1 = \begin{bmatrix} C_1 & C_2^\parallel(\cos q_x + \cos q_y) \\ C_2^{\parallel*}(\cos q_x + \cos q_y) & C_1 \end{bmatrix}, \quad \mathcal{H}_2 = C_2^\perp \cos q_z \begin{bmatrix} 1 & 0 \\ 0 & 1 \end{bmatrix}, \tag{B3}$$

and

$$\mathcal{H}^b(\mathbf{q}) = \begin{bmatrix} \mathcal{H}_3 & \mathcal{H}_4 \\ \mathcal{H}_4 & \mathcal{H}_3 \end{bmatrix}, \quad \mathcal{H}_3 = (C_3^{\parallel} \cos q_x + C_3^{\parallel*} \cos q_y) \begin{bmatrix} 0 & 1 \\ 1 & 0 \end{bmatrix}, \quad \mathcal{H}_4 = \cos q_z \begin{bmatrix} C_3^{\perp} & 0 \\ 0 & C_3^{\perp*} \end{bmatrix}. \quad (\text{B4})$$

[Note that  $C_1$  and  $C_2^{\perp}$  are real, see Appendix A.]

Let us now denote the boson fields in which the Hamiltonian (17) is diagonalized by  $\tau_{\ell}(\mathbf{q})$ ,  $\ell = 1, 2, 3, 4$ . These fields are related to the original ones,  $\xi_{\ell}(\mathbf{q})$ , by the general linear transformation

$$\tau_{\ell}(\mathbf{q}) = \sum_j P_{\ell j}(\mathbf{q}) \xi_j(\mathbf{q}) - \sum_j Q_{\ell j}(\mathbf{q}) \xi_j^{\dagger}(-\mathbf{q}), \quad (\text{B5})$$

with

$$\sum_j \left( P_{\ell j}(\mathbf{q}) P_{nj}^*(\mathbf{q}) - Q_{\ell j}(\mathbf{q}) Q_{nj}^*(\mathbf{q}) \right) = \delta_{n\ell}, \quad \sum_j \left( -P_{\ell j}(\mathbf{q}) Q_{nj}(-\mathbf{q}) + Q_{\ell j}(\mathbf{q}) P_{nj}(-\mathbf{q}) \right) = 0, \quad (\text{B6})$$

for the  $\tau$  fields to obey the boson commutation relations. In order that the  $\tau$  fields will represent normal modes, they have to satisfy

$$\left[ \tau_{\ell}(\mathbf{q}), h_{\text{SW}}(\mathbf{q}) \right] = \Omega_{\ell}(\mathbf{q}) \tau_{\ell}(\mathbf{q}), \quad (\text{B7})$$

where  $\Omega_{\ell}(\mathbf{q})$ ,  $\ell = 1, 2, 3, 4$  are the eigenfrequencies of our spin-wave Hamiltonian. Inserting Eqs. (B5) into Eq. (B7), and equating the coefficients of  $\xi$  and  $\xi^{\dagger}$  on both sides, we obtain

$$\begin{aligned} \Omega_{\ell}(\mathbf{q}) P_{\ell j}(\mathbf{q}) &= \sum_n \left( P_{\ell n}(\mathbf{q}) \mathcal{H}_{nj}^a(\mathbf{q}) + Q_{\ell n}(\mathbf{q}) \mathcal{H}_{nj}^{b*}(\mathbf{q}) \right), \\ -\Omega_{\ell}(\mathbf{q}) Q_{\ell j}(\mathbf{q}) &= \sum_n \left( Q_{\ell n}(\mathbf{q}) \mathcal{H}_{nj}^{a*}(\mathbf{q}) + P_{\ell n}(\mathbf{q}) \mathcal{H}_{nj}^b(\mathbf{q}) \right). \end{aligned} \quad (\text{B8})$$

Identifying  $P_{\ell j} \equiv v_j^{\ell}$  as “vector number  $\ell$  whose entries are  $j$ ”, and similarly for  $Q_{\ell j} \equiv u_j^{\ell}$  we arrive at the equations

$$\Omega_{\ell} v^{\ell} = \mathcal{H}^{a*} v^{\ell} + \mathcal{H}^{b*} u^{\ell}, \quad -\Omega_{\ell} u^{\ell} = \mathcal{H}^a u^{\ell} + \mathcal{H}^b v^{\ell}, \quad (\text{B9})$$

where we have dropped the explicit  $\mathbf{q}$  dependence for brevity. From the first of Eqs. (B6), we have

$$|v^{\ell}|^2 - |u^{\ell}|^2 = 1, \quad (\text{B10})$$

where  $u^{\ell}$  and  $v^{\ell}$  are 4-dimensional vectors.

We split the 4-dimensional vectors  $u^{\ell}$  and  $v^{\ell}$  into two 2-dimensional vectors,  $u^{\ell} = (u_1^{\ell}, u_2^{\ell})$ ,  $v^{\ell} = (v_1^{\ell}, v_2^{\ell})$ , and write explicitly Eqs. (B9), using the definitions (B3) and (B4). The resulting equations may be arranged in the form

$$\begin{aligned} -\Omega(u_1 - u_2) &= (\mathcal{H}_1 - \mathcal{H}_2)(u_1 - u_2) + (\mathcal{H}_3 - \mathcal{H}_4)(v_1 - v_2), \\ \Omega(v_1 - v_2) &= (\mathcal{H}_1^* - \mathcal{H}_2)(v_1 - v_2) + (\mathcal{H}_3^* - \mathcal{H}_4^*)(u_1 - u_2), \\ -\Omega(u_1 + u_2) &= (\mathcal{H}_1 + \mathcal{H}_2)(u_1 + u_2) + (\mathcal{H}_3 + \mathcal{H}_4)(v_1 + v_2), \\ \Omega(v_1 + v_2) &= (\mathcal{H}_1^* + \mathcal{H}_2)(v_1 + v_2) + (\mathcal{H}_3^* + \mathcal{H}_4^*)(u_1 + u_2), \end{aligned} \quad (\text{B11})$$

where we have also dropped the index  $\ell$  for brevity. It is thus seen that there are two types of solutions: Either  $u_1 = u_2$  and  $v_1 = v_2$ , in which case the first couple of equations is trivially satisfied, and it is needed to solve just the second pair of equations, or *vice versa*:  $u_1 = -u_2$  and  $v_1 = -v_2$  and then the first pair of equations has to be solved. However, the only difference between the first pair of equations and the second one are the signs appearing in front of  $\mathcal{H}_2$  and  $\mathcal{H}_4$ . Glancing at Eqs. (B3) and (B4) reveals that these signs are determined just by  $\cos q_z$ . Therefore, it suffices to solve one pair of equations, and the solution of the second is obtained by simply changing the sign of  $\cos q_z$ . Focusing on the first option, we find that two of the eigenfrequencies are determined by

$$\det \begin{bmatrix} C_1 + C_2^{\perp} \cos q_z + \Omega & C_2^{\parallel} (\cos q_x + \cos q_y) & C_3^{\perp} \cos q_z & C_3^{\parallel} \cos q_x + C_3^{\parallel*} \cos q_y \\ C_2^{\parallel*} (\cos q_x + \cos q_y) & C_1 + C_2^{\perp} \cos q_z + \Omega & C_3^{\parallel} \cos q_x + C_3^{\parallel*} \cos q_y & C_3^{\perp*} \cos q_z \\ C_3^{\perp*} \cos q_z & C_3^{\parallel*} \cos q_x + C_3^{\parallel} \cos q_y & C_1 + C_2^{\perp} \cos q_z - \Omega & C_2^{\parallel*} (\cos q_x + \cos q_y) \\ C_3^{\parallel*} \cos q_x + C_3^{\parallel} \cos q_y & C_3^{\perp} \cos q_z & C_2^{\parallel} (\cos q_x + \cos q_y) & C_1 + C_2^{\perp} \cos q_z - \Omega \end{bmatrix} = 0. \quad (\text{B12})$$

The modes  $\Omega_2(\mathbf{q})$  and  $\Omega_4(\mathbf{q})$  [see Eqs. (19)] are the positive roots of the fourth-order polynomial in  $\Omega$  given by Eq. (B12). The other two eigenfrequencies are found by changing the sign of  $\cos q_z$ .

TABLE I. The single-bond spin-exchange couplings (in meV). The symmetric anisotropies are given as  $\mathbf{A}_{mn}^d = (A_{mn}^{xx}, A_{mn}^{yy}, A_{mn}^{zz})$  and  $\mathbf{A}_{mn}^{od} = (A_{mn}^{yz}, A_{mn}^{xz}, A_{mn}^{xy})$  for the diagonal and off-diagonal entries, respectively.

Heisenberg couplings
$J_{12} = 17.094, J_{13} = 13.484$
Moriya vectors
$\mathbf{D}_{12} = (2.260, -0.884, -0.893), \mathbf{D}_{13} = (-2.207, 0.377, 0)$
Symmetric anisotropies
$\mathbf{A}_{12}^d = (0.131, 0, 0), \mathbf{A}_{13}^d = (-0.027, 0, 0),$ $\mathbf{A}_{12}^{od} = (0, -0.077, -0.061), \mathbf{A}_{13}^{od} = (0, 0, -0.052)$

TABLE II. The macroscopic couplings of the sublattice magnetizations in terms of the microscopic single-bond spin couplings. For instance,  $I_{12} = J_{12}$  but  $I_{13} = J_{13}/2$ , because the coordination number of a Ti ion is 4 in the planes and 2 between the planes.

Isotropic couplings
$I_{12} = J_{12}, I_{13} = \frac{1}{2}J_{13}$
Dzyaloshinskii vectors
$\mathbf{D}_{12}^D = (0, D_{12}^y, D_{12}^z), \mathbf{D}_{13}^D = \frac{1}{2}\mathbf{D}_{13}$
Macroscopic symmetric anisotropies
$\Gamma_{12}^d = \mathbf{A}_{12}^d, \Gamma_{12}^{od} = (A_{12}^{yz}, 0, 0), \Gamma_{13} = \frac{1}{2}A_{13}$

TABLE III. Symmetries of the magnetic Hamiltonian due to the space group. The relations for the anisotropic couplings are abbreviated as follows:  $(+, +, +)_{12} = (-, +, +)_{16}$  means that  $\mathbf{D}_{12}^D = (-D_{16}^x, D_{16}^y, D_{16}^z)$ , etc. Due to the glide planes, the Dzyaloshinskii vectors of the planar bonds have vanishing  $x$  components, and the respective symmetric anisotropies have vanishing  $xz$  and  $xy$  entries. Because of the mirror planes, the Dzyaloshinskii vectors of the inter-planar bonds have vanishing  $z$  components and the respective symmetric anisotropies have vanishing  $yz$  and  $xz$  entries.

Isotropic couplings
$I_{12} = I_{34}, I_{13} = I_{24}$
Dzyaloshinskii vectors
$(0, +, +)_{12} = (0, -, +)_{34}, (+, +, 0)_{13} = (+, -, 0)_{24}$
Macroscopic symmetric anisotropies
$(+, 0, 0)_{12} = (-, 0, 0)_{34}, (0, 0, +)_{13} = (0, 0, -)_{24}$

TABLE IV. The structure of the magnetic order, characterized by the sublattice magnetizations  $\mathbf{M}_i$  in the classical ground state (normalized to  $M$ ), in terms of the canting angles  $\varphi$  and  $\vartheta$ . We use orthorhombic coordinates, in which the  $x, y, z$  axes are oriented along the crystallographic  $a, b, c$  directions.

$x$ components: G-type
$-M_1^x = M_2^x = M_3^x = -M_4^x = M \cos \varphi \cos \vartheta$
$y$ components: A-type
$-M_1^y = -M_2^y = M_3^y = M_4^y = M \sin \varphi \cos \vartheta$
$z$ components: ferromagnetic
$M_1^z = M_2^z = M_3^z = M_4^z = M \sin \vartheta$
Calculated values of the canting angles
$\varphi = 1.42^\circ, \vartheta = 0.80^\circ$

<sup>1</sup> B. Keimer, D. Casa, A. Ivanov, J. W. Lynn, M. v. Zimmermann, J. P. Hill, D. Gibbs, Y. Taguchi, and Y. Tokura, Phys. Rev. Lett. **85**, 3946 (2000).

<sup>2</sup> M. Cwik, T. Lorenz, J. Baier, R. Müller, G. André, F. Bourée, F. Lichtenberg, A. Freimuth, R. Schmitz, E. Müller-Hartmann, and M. Braden, Phys. Rev. B **68**, 060401(R) (2003).

<sup>3</sup> G. Khaliullin and S. Maekawa, Phys. Rev. Lett. **85**, 3950 (2000).

<sup>4</sup> K. I. Kugel and D. I. Khomskii, Fiz. Tverd. Tela (Leningrad) **17**, 454 (1975) [Sov. Phys. Solid State **17**, 285 (1975)]; Usp. Fiz. Nauk **136**, 621(1982) [Sov. Phys. Usp. **25**, 231 (1982)].

<sup>5</sup> A. B. Harris, T. Yildirim, A. Aharony, O. Entin-Wohlman, and I. Ya. Korenblit, Phys. Rev. Lett. **91**, 087206 (2003).

<sup>6</sup> A. B. Harris, T. Yildirim, A. Aharony, O. Entin-Wohlman, and I. Ya. Korenblit, Phys. Rev. B **69**, 035107 (2004).

<sup>7</sup> M. Haverkort, Z. Hu, A. Tanaka, G. Ghiringhelli, H. Roth, M. Cwik, T. Lorenz, C. Schuessler-Langeheine, S. V. Streltsov, A. S. Mylnikova, V. I. Anisimov, C. de Nadaï, N. B. Brookes, H. H. Hsieh, H.-J. Lin, C. T. Chen, T. Mizokawa, Y. Taguchi, Y. Tokura, D. I. Khomskii, and L. H. Tjeng, cond-mat/0405516 (2004).

<sup>8</sup> A. Gößling, M. Grüninger, B. Keimer, and C. Ulrich, private communication.

<sup>9</sup> T. Kiyama and M. Itoh, Phys. Rev. Lett. **91**, 167202 (2003).

<sup>10</sup> P. Lunkenheimer, T. Rudolf, J. Hemberger, A. Pimenov, S. Tachos, F. Lichtenberg, and A. Loidl, Phys. Rev. B **68**, 245108 (2003).

- <sup>11</sup> R. Schmitz, O. Entin-Wohlman, A. Aharony, A. B. Harris, and E. Müller-Hartmann, submitted to Phys. Rev. B, cond-mat/0407524 (2004).
- <sup>12</sup> As compared to Ref. 11, we have slightly modified some of the numerical values employed in the calculation of the single-bond spin couplings: The effective Ti–O charge-transfer energy used here is  $\Delta_{\text{eff}} = 6.6$  eV instead of the value 5.5 eV used in Ref. 11. (Hence the spin-exchange couplings are multiplied by  $(5.5/6.6)^2 = 0.694$  compared to the ones of that reference. This corresponds to a renormalization of the units in which the ground-state energy is found, but does not affect the minimization of that energy, and consequently, does not modify the ground-state magnetization configuration.) In addition, the spin-exchange couplings are computed taking into account only systematic contributions in powers of the spin-orbit coupling.<sup>11</sup>
- <sup>13</sup> T. Holstein and H. Primakoff, Phys. Rev. **58**, 1098 (1940).
- <sup>14</sup> D. Reznik, P. Bourges, H. F. Fong, L. P. Regnault, J. Bossy, C. Vettier, D. L. Milius, I. A. Aksay, and B. Keimer, Phys. Rev. B **53**, R14741 (1996).
- <sup>15</sup> S. M. Hayden, G. Aeppli, T. G. Perring, H. A. Mook, and F. Dogan, Phys. Rev. B **54**, R6905 (1996).
- <sup>16</sup> S. Pailhes, Y. Sidis, P. Bourges, C. Ulrich, V. Hinkov, L. P. Regnault, A. Ivanov, B. Liang, C. T. Lin, C. Bernhard, and B. Keimer, Phys. Rev. Lett. **91**, 237002 (2003).
- <sup>17</sup> B. Keimer, private communication.
- <sup>18</sup> T. A. Kaplan, Z. Phys. **B 49**, 313 (1983).
- <sup>19</sup> L. Shekhtman, O. Entin-Wohlman, and A. Aharony, Phys. Rev. Lett. **69**, 836 (1992).
- <sup>20</sup> O. Entin-Wohlman, A. Aharony, and L. Shekhtman, Phys. Rev. B **50**, 3068 (1994).